FAR-INFRARED AND SUBMILLIMETER WAVELENGTH OBSERVATIONS OF STAR-FORMING DENSE CORES. II. IMAGES

E. F. LADD[1,2,3]
Harvard-Smithsonian Center for Astrophysics, MS-42, 60 Garden Street, Cambridge, MA 02138

FRED C. ADAMS[3]
Harvard-Smithsonian Center for Astrophysics, MS-51, 60 Garden Street, Cambridge, MA 02138

S. CASEY[1,2]
NASA Goddard Space Flight Center, Code 685, Greenbelt, MD 20771

J. A. DAVIDSON[1,2]
NASA Ames Research Center, Moffett Field, CA 94035

G. A. FULLER[3]
Harvard-Smithsonian Center for Astrophysics, MS-42, 60 Garden Street, Cambridge, MA 02138

D. A. HARPER[1,2]
Yerkes Observatory, Williams Bay, WI 53191

P. C. MYERS[1,2,3]
Harvard-Smithsonian Center for Astrophysics, MS-42, 60 Garden Street, Cambridge, MA 02138

AND

R. PADMAN[3]
University of Cambridge, Cavendish Laboratory, Madingley Road, Cambridge, CB3 0HE, England, UK

ABSTRACT

This paper reports on far-infrared and submillimeter wavelength observations of low-mass protostellar candidates. The data set comprises emission maps of nine sources observed over a wavelength range 100–800 μm. The emission is extended at all wavelengths longer than 100 μm. The apparent size of the emission regions is weakly correlated with the beam size and is consistent with an underlying specific intensity profile which is scale-free (i.e., I_ν decreases as a power law with distance). The observed emission maps are not circular, but have a mean aspect ratio of 1.3, and the position angles are similar to those determined from maps of molecular emission. The observational results are used in conjunction with theoretical considerations to constrain the physical properties of the putative protostellar envelopes. The best constrained parameter is the sum $p + q$ of the power-law indices of the density and temperature distributions; this sum is shown to lie in the range $1.8 \leq p + q \leq 2.3$ for the sources L1489 and L1527.

Subject headings: spectrophotometry — stars: circumstellar shells — stars: pre–main-sequence

1. INTRODUCTION

During the last decade, both observational and theoretical studies have shown that stars generally form within condensations of gas and dust in interstellar space (see, e.g., Shu, Adams, & Lizano 1987 for a review). These regions, called dense cores, are characterized by high visual opacity and molecular line emission from species which are collisionally excited at densities greater than 10^4 H cm^{-3} (Benson & Myers 1989). Within these cores, embedded sources with luminosities characteristic of low-mass stars ($L \sim 1$–$10\ L_\odot$) but with much "colder" spectra are often found (Beichman et al. 1986). These sources typically emit the bulk of their radiant energy into the

far-infrared and submillimeter (60 μm $< \lambda < 1000$ μm) rather than in the visible. They are prestellar objects and probably derive the bulk of their energy output from the gravitational infall of material from the surrounding core (Adams, Lada, & Shu 1987).

The most successful theories of the early stages of star formation involve the accretion via an "inside-out" collapse of an isothermal sphere (Larson 1969; Shu 1977), where the material in the inner parts of the sphere becomes gravitationally unstable before the material in the outer regions. More detailed models of this infall solution predict a specific spectral and spatial distribution of energy within these cores (Adams & Shu 1986; Adams, Lada, & Shu 1987; Wolfire & Cassinelli 1987).

In an earlier work (Ladd et al. 1991, hereafter Paper I), we have compared the observed broad-band spectral energy distribution of several sources with the predictions of core models over three orders of magnitude in frequency. We found that the observed spectral energy distributions are in basic agreement with the predictions of the theory, but that nonspherical structure may play an important role in shaping the near-infrared

---

[1] Visiting Astronomer at the NASA Kuiper Airborne Observatory.
[2] Visiting Astronomer at the NASA Infrared Telescope Facility, which is operated by the University of Hawaii under contract with the National Aeronautics and Space Administration.
[3] Visiting Astronomer at the James Clerk Maxwell Telescope, which is operated by the Royal Observatory Edinburgh on behalf of the Science and Engineering Research Council of the United Kingdom, the Netherlands Organization for Scientific Research, and the National Research Council of Canada.

555

spectrum. In this present work, we describe the spatial profiles of the far-infrared and submillimeter emission from these sources. We present mapping results for nine regions forming low- to intermediate-mass stars, all of which show some evidence of extended emission. The structure of this extended emission suggests that the underlying specific intensity profile is scale-free. Furthermore, our results indicate that much of the far-infrared and submillimeter emission is emitted from the outer core, which absorbed protostellar photons and reprocessed them to longer wavelengths.

Extended far-infrared and submillimeter emission has been observed in only a few other low-luminosity sources. Walker, Adams, & Lada (1990) have shown that the spatial profile of 1 mm emission from the $IRAS$ source 04286+1801 in L1551 is more extended than their telescope beam and is consistent with the protostellar models of Adams & Shu (1986); more recently Butner et al. (1991) have shown that the profile of the same source is extended at 100 μm. Yamashita et al. (1990) find evidence for an extended distribution of dust around the 20,000 $L_\odot$ infrared source GGD 27 and have compared the size of the submillimeter emission region with a model consisting of a power-law distribution of temperature and density.

In this paper, we show that extended far-infrared and submillimeter emission is present in many protostellar sources. The mapping observations are discussed in § 2, along with an analysis of the beam shapes of each observation. In § 3 we discuss the size and shape of the long-wavelength emission from our sources and show that the emission profiles are extended in our beams. We discuss the nature of the extended emission and a recipe for determining the underlying physical structure of the cores in § 4. Our results and conclusions are summarized in § 5.

2. OBSERVATIONS

The observations presented here are submillimeter and far-infrared continuum maps made using a variety of telescopes. The observation dates and telescopes used are listed in Table 1A. The instrumental parameters are summarized in Table 1B.

Three of nine sources were observed with the James Clerk Maxwell Telescope (JCMT) using the common-user instrument UKT-14, a single element germanium bolometer (Ade et al. 1984), in a chopped raster scanning mode. The chopper spacing was 40″ in azimuth for all observations, and the raster scans typically sampled 4 square arcminutes of the sky. Broadband filters centered on 450, 800, and 1100 μm were used during the observations. The maps were reconstructed from those data using the NOD2 software package, originally developed by Haslam (1974) and adapted for use at the JCMT. The resulting maps have an effective chopper throw of the size of the mapped region, typically $\sim 2'$ for our data.

The rest of the observations listed in Table 1A were acquired using the Yerkes Observatory Array Cameras, each consisting of a 32 element array of helium cooled silicon bolometers. Each detector is mounted in an integrating cavity and illuminated through compound parabolic cones with a beam of $\sim 45''$ (see Hildebrand 1986; Harper et al. 1976). At wavelengths shorter than 200 μm, we observed with the NASA Kuiper Airborne Observatory (KAO); the 350 μm data were observed with the NASA Infrared Telescope Facility (IRTF). In all observations we employed a 5′ chopper throw, rotated so that we chopped into regions of low visual obscuration. Further information regarding the observations can be found in Paper I.

2.1. Flux Calibration

Calibration was accomplished by comparison of source fluxes to the fluxes of planets or other bright known calibrators. At the JCMT, calibration and atmospheric correction were obtained from frequent observations of Mars, Jupiter, and the point sources HL Tau and CRL 618. The Martian fluxes were taken from Ulrich (1981) and Jovian fluxes from Griffin et al. (1986). The fluxes for HL Tau and CRL 618 were determined from comparison with the planetary measurements and found to be consistent with the observations of Sandell (1989) and Adams, Emerson, & Fuller (1990). The IRTF observations were calibrated by frequent comparison with M42 and Jupiter. On the KAO, attenuation by water vapor was tracked

TABLE 1
A. Observations

Core Name	Right Ascension[a] (1950)	Declination[a] (1950)	Date Observed	Telescope[b]	Wavelength (μm)
L1489	04:01:40.6	26:10:49	1987 Mar	KAO	100, 160
			1987 Oct	IRTF	350
			1989 Jan	JCMT	800
L1535	04:32:31.5	24:02:07	1987 Sep	KAO	100, 160
L1527	04:36:48[c]	25:57:05	1987 Mar	KAO	100, 160
			1987 Oct	IRTF	350
			1989 Jan	JCMT	450, 800
L43	16:31:37.7	−15:40:52	1989 May	KAO	150, 190
L483	18:14:50.6	−04:40:49	1988 May	KAO	100, 160, 190
L673B	19:18:01.3	11:16:27	1988 May	KAO	160, 190
L673A	19:18:04.6	11:14:12	1988 May	KAO	100, 160, 190
L1172A	21:01:44.2	67:42:24	1988 May	KAO	100, 160
L1031B	21:45:27.9	47:18:12	1988 May	KAO	100, 160
			1989 May	KAO	190
			1987 Oct	IRTF	350
			1989 Oct	JCMT	800

[a] The pointing centers for the maps are taken from Myers et al. 1987 where available, or the $IRAS$ Point Source Catalog.
[b] KAO: NASA Kuiper Airborne Observatory, Moffett Field, CA. IRTF: NASA Infrared Telescope Facility, Mauna Kea, HI. JCMT: James Clerk Maxwell Telescope, Mauna Kea, HI.
[c] The right ascension for L1527 was listed incorrectly in Table 1A of Paper I.

TABLE 1

B. Instrumental Parameters

Telescope	Backend	Filter (μm)	v_{eff}[a] (GHz)	Δv[a] (GHz)	Field of View	Sensitivity[b] (Jy beam^{-1})	Chopper Throw
KAO	Yerkes 32 element bolometer	100	3105	1348	300″	4	300″
		160	1670	522	300	5	300
		190	1351	392	300	5	300
IRTF	Yerkes 32 element bolometer	350	772	394	300	1	300
JCMT	UKT-14 bolometer	450	685	84	120[c]	0.2	120[d]
		800	394	103	120[c]	0.1	120[d]

[a] Effective frequency and width are determined for a flat spectral source and no attenuating water vapor. The values for v_{eff} are the transmission-weighted mean frequencies, except for the JCMT values, which are the average of the two frequencies where the filter response is 60% of maximum.

[b] Typical 1 σ noise levels for the mapping data presented here.

[c] The JCMT field of view is determined by the size of the map made. These values are typical of our maps.

[d] The actual chopper throw was 60″, but the map was raster scanned in the chopper direction and later reconstructed with NOD2 analysis software, creating an effective chop of 120″.

by facility water vapor radiometers and at the IRTF and JCMT by frequent observations of calibration sources Mars, Jupiter, M82, and W51. The absolute uncertainty in the map flux densities is estimated to be 30%–40%, due to the uncertainty in the calibrator fluxes and the atmospheric attenuation.

For the purposes of this paper, in which we discuss the shape and extent of the observed sources, absolute calibration is not as critical as the relative "point-to-point" calibration across the map. In all cases, the data were oversampled by at least a factor of 2 in both spatial dimensions, and then convolved to enhance the signal-to-noise ratio. We have quantified the point-to-point uncertainties by measuring the differences between measurements separated on the sky by less than one FWHM beam. For two such measurements, the signal contributions will be highly correlated, while the noise contributions will not. We use the standard deviation of a group of these differences as the relative point-to-point error and list them in Table 2.

2.2. Beam-Size Calibration

In this work we will discuss the extended nature of the emission from our sources, and in many cases, the source extent is not much greater than the extent of the beams used. Therefore, it is critical that we understand the size and shape of the beam for each telescope configuration used.

To determine the shape of the beam in our observations, we observed Jupiter or Mars in each of the observing configurations, except with the KAO at 190 μm. Jupiter was observed during the 1987 September KAO flight series and also at the IRTF in 1987 October. Mars was observed during all of the JCMT observations. In all cases, the planets and sources were observed and analyzed in the same way.

The beam size is determined by three major factors in the KAO and IRTF observations. First, the diffraction limit of the telescope used establishes a minimum beam size. Second, the Winston field concentrators in front of each detector in the Dewar assembly admit radiation through a 45″ aperture, further broadening the beam. Finally, the resulting data have been smoothed to enhance the signal-to-noise ratio. The JCMT observations are likewise affected, except that the detector throughput is controlled by a focal-plane diaphragm illuminating the single UKT-14 bolometer.

We have calculated the beam sizes from the planetary obser-

vations by comparing the planetary maps with models of each planet's intensity profile convolved with an estimate of the system point spread function. We calculate the point spread function as the convolution of the telescope response (assumed an Airy function), the focal-plane grading function (a "pillbox," or radial step function was assumed), and the software con-

TABLE 2

Far-Infrared and Submillimeter Flux Densities

Core Name	Wavelength (μm)	Single-Beam Flux (Jy)	1″ Flux (Jy)	Map rms[a] (Jy)
L1489........	100	55	74	5.3
	160	46	56	3.0
	350	4.8	8.4	0.8
	800	0.3	1.5	0.08
L1535........	100	24	31	4.4
	160	38	45	4.6
L1527........	100	47	89	4.3
	160	69	94	6.2
	350	12	22	1.1
	450	3.2	14	0.2
	800	0.5	1.4	0.08
L43	160	70	79	5.7
	190	38	38	4.7
L483[b]	100	130	170	6.7
	160	270	290	6.7
	190	160	140	7.8
L673B	100	19	19	2.9
	160	33	49	5.7
	190	44	36	7.8
L673A	100	11	15	2.9
	160	56	69	2.7
	190	53	54	5.4
L1172A	100	10	11	2.2
	160	6	10	1.5
L1031B	100	67	80	5.1
	160	86	100	4.0
	190	110	120	5.0
	350	5.4	7.7	1.4
	800	0.3	1.5	0.02

[a] The map rms values give only the random component of the uncertainty in our maps. These values are not the total errors in the measured fluxes listed above. The above measurements are also subject to systematic errors of 30%–40%.

[b] These values for L483 are subject to larger than normal systematic errors due to the lack of accurate water vapor information on two KAO flights. The errors in these fluxes are 40%–50%.

TABLE 3

BEAM COMPONENTS

| | | | COMPONENTS OF THE BEAM | | | | | |
TELESCOPE	BACKEND	WAVELENGTH (μm)	Airy pattern (FWHM)	Aperture (diameter)	Smoothing (FWHM)	PLANET (diameter)	PLANET IMAGE (FWHM)	BEAM SIZE[a] (FWHM)
KAO	Yerkes 32 element	100	27.5	45	24	48	56	45 ± 3.1
	bolometer	100	44	45	24	48	62	50 ± 2.9
		190	52.3	45	24	...	...	58
IRTF	Yerkes 32 element bolometer	350	29.3	45	24	48	56	45 ± 2.0
JCMT	UKT 14 bolometer	450	7.5	16.8	...	7.6	17	15 ± 0.7[b]
		800	13.4	16.8	...	7.6	17	17 ± 1.2

NOTE.—All beam component sizes are given in arcseconds.

[a] The error listed with each derived value is the root mean square of the difference between the calculated and observed profiles. There is no error listed for the 190 μm beam size estimate because Jupiter was not observed in this configuration.

[b] The shape of the 450 μm beam is assumed to be Gaussian and not the convolution of the Airy disk, aperture, and smoothing functions (see text).

volving function (a Gaussian). The FWHM sizes of each contribution to the beam for each system are shown in Table 3.

We then convolve this point spread function with the spatial intensity profile of Jupiter or Mars (assumed in each case to be a flat disk) and compare with the observed data. In Figure 1, the observed profile of Jupiter is compared with the expected profile of a 48″ disk with the Yerkes Camera on the KAO and IRTF. In Figure 2, the observed profile of Mars is compared with the expected profile of 7.″6 disk seen with the UKT-14

system on the JCMT. In both figures, the point spread function is shown as a dashed line.

Our calculated beams appear to fit well with the observed data, except at 450 μm where the profiles differ significantly (Fig. 2a). The *calculated* profile is dominated by the sharp response of the aperture function, largely because the Airy pattern of a 15 m telescope at 450 μm has a FWHM of only 7″. However, the data appear to be less centrally concentrated
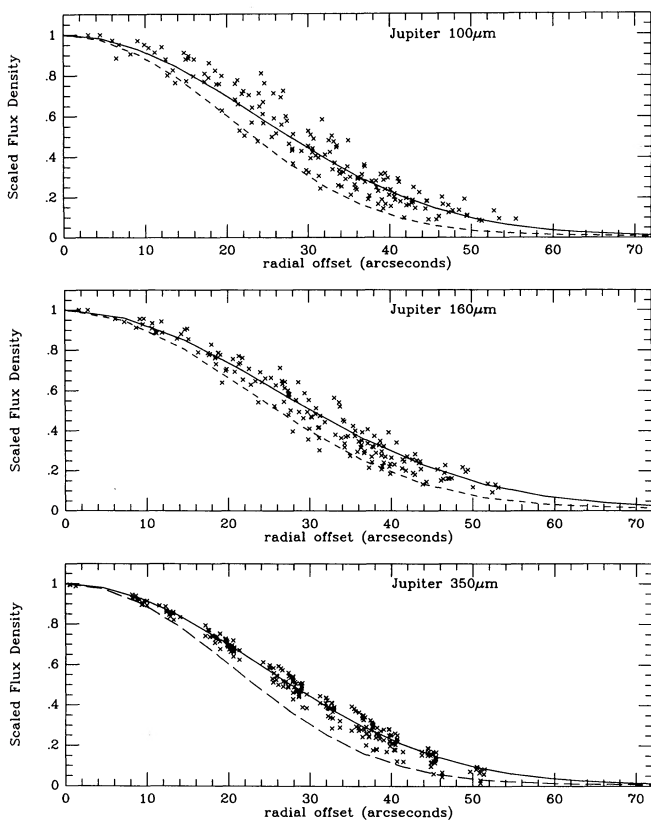

FIG. 1.—Observations of Jupiter as a function of offset from peak position at 100, 160, and 350 μm. Solid line represents the expected profile of Jupiter using the observing method described in the text. Dashed line is the point spread function for this observing configuration.
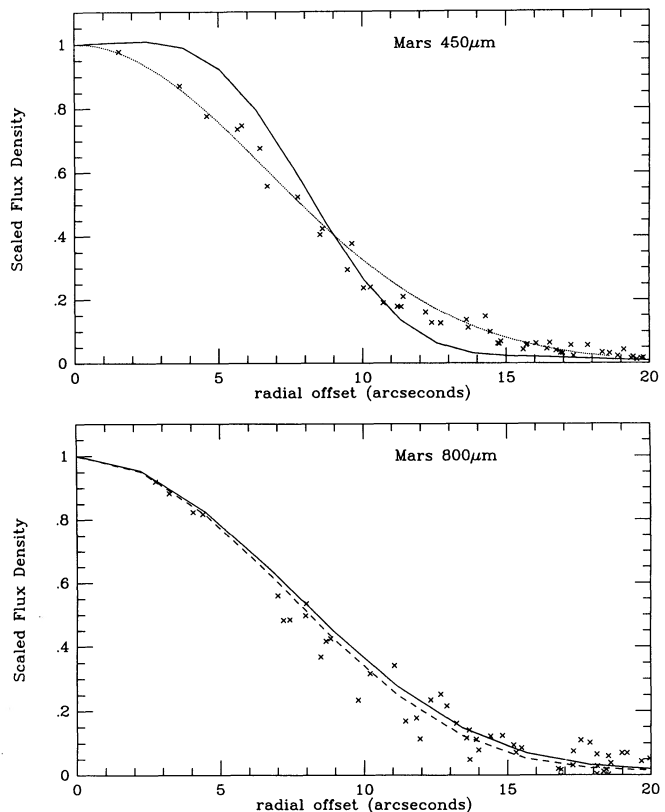

FIG. 2.—Observations of Mars as a function of offset from peak position at 450 and 800 μm. Solid line represents the expected profile of Mars using the observing method described in the text. Since the 450 μm data are not well fitted by our model, we will use a 15″ Gaussian point spread function (*dotted line*). The 800 μm data are well fitted by our model, and the derived point spread function is plotted as a dashed line.

than expected. This is consistent with degradation of the beam caused by deviations of the telescope surface from an ideal parabolic profile—at the time of the observations the rms surface error is believed to have been ~ 40 μm, and measurements have shown that the beam has the form of a central diffraction "spike" with an extended "error pattern" (Lasenby & Hills 1991). Here we note that the observed profile of Mars is well reproduced by a Gaussian beam of FWHM 15" convolved with a 7".6 disk (see Fig. 2a). We therefore use a 15" Gaussian as our estimate of the point spread function at 450 μm.

We made no observation of Jupiter at 190 μm using the KAO. However, given that the system used for the 190 μm measurements was also used at 100 and 160 μm, we simply extrapolate those results to determine the 190 μm beam size. Using the Airy function corresponding to the longer wavelength and convolving it with the aperture response function and smoothing function as above, we derive a FWHM beam size of 58" for the 190 μm observations.

Table 3 contains the FWHM sizes of the calculated point spread functions. The derived values do not differ significantly from other published beam size estimates obtained with same equipment (see, e.g., Davidson 1987; Sandell 1989).

3. RESULTS

The far-infrared and submillimeter images are shown in Figures 3–10. In all except two maps, an emission peak is located within one map beam of the *IRAS* Point Source position. The emission peaks in the 450 and 800 μm maps of L1527 are located ~ 1.5 beams ($\sim 30''$) from the *IRAS* position. However, they are coincident with the emission peaks measured at 100 and 350 μm. We suspect that the *IRAS* position, which in this case is determined by only the 60 and 100 μm detections (because the source was not detected at 12 and 25 μm), is probably in error.

While the 100 μm maps are largely circularly symmetric, the maps of the longer wavelength emission show significant additional structure. The maps of L673A and B, L1489, and L43, show long-wavelength emission connecting two distinct emission centers. In L673, each emission peak is associated with an *IRAS* Point Source, but the subsidiary emission peaks toward L1489 at 350 μm and toward L43 at 190 μm have no *IRAS* counterpart. These emission peaks may identify extremely cold ($T \sim 10$ K) clumps which are similar to their star-forming neighbors but do not contain an embedded star.

3.1. Sizes

We have not convolved all of our maps to a common beam size equal to the largest beam in our data set (the 58" beam of the 190 μm measurements), because we intend to make use of the higher spatial resolution where available. To quantify the geometry of these sources, we have fitted an elliptical Gaussian plus baseline model to each of the maps. The results of this
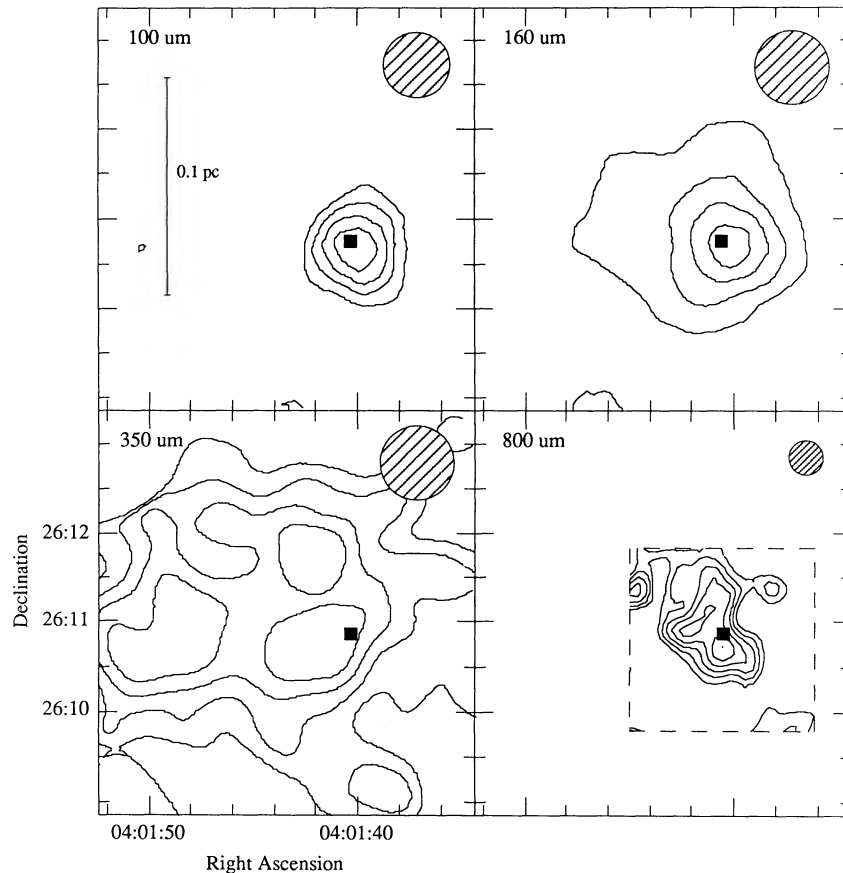

FIG. 3.—Maps of L1489 at 100, 160, 350, and 800 μm. Maps are co-aligned, and the coordinates of the lower left box apply to all images. FWHM beam size is given by the hatched circle in each observation. Lowest contour level and contour increments are 10 Jy beam^{-1} and 10 Jy beam^{-1} for the 100 and 160 μm maps, 1.0 Jy beam^{-1} and 1.0 Jy beam^{-1} for the 350 μm map, and 0.05 Jy beam^{-1} and 0.05 Jy beam^{-1} for the 800 μm map. Filled squares mark the 2 μm position found by Myers et al. (1987).
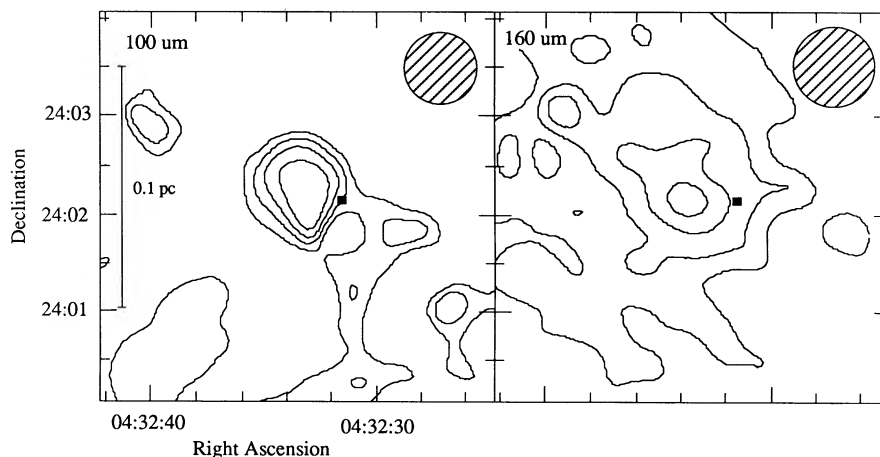
FIG. 4.—Maps of L1535 at 100 and 160 μm. Labels are the same as in Fig. 3. Lowest contour level and contour increments are 5 Jy beam^{-1} and 5 Jy beam^{-1} for the 100 μm map and 10 Jy beam^{-1} and 10 Jy beam^{-1} for the 160 μm map. Filled squares mark the *IRAS* Point Source position.
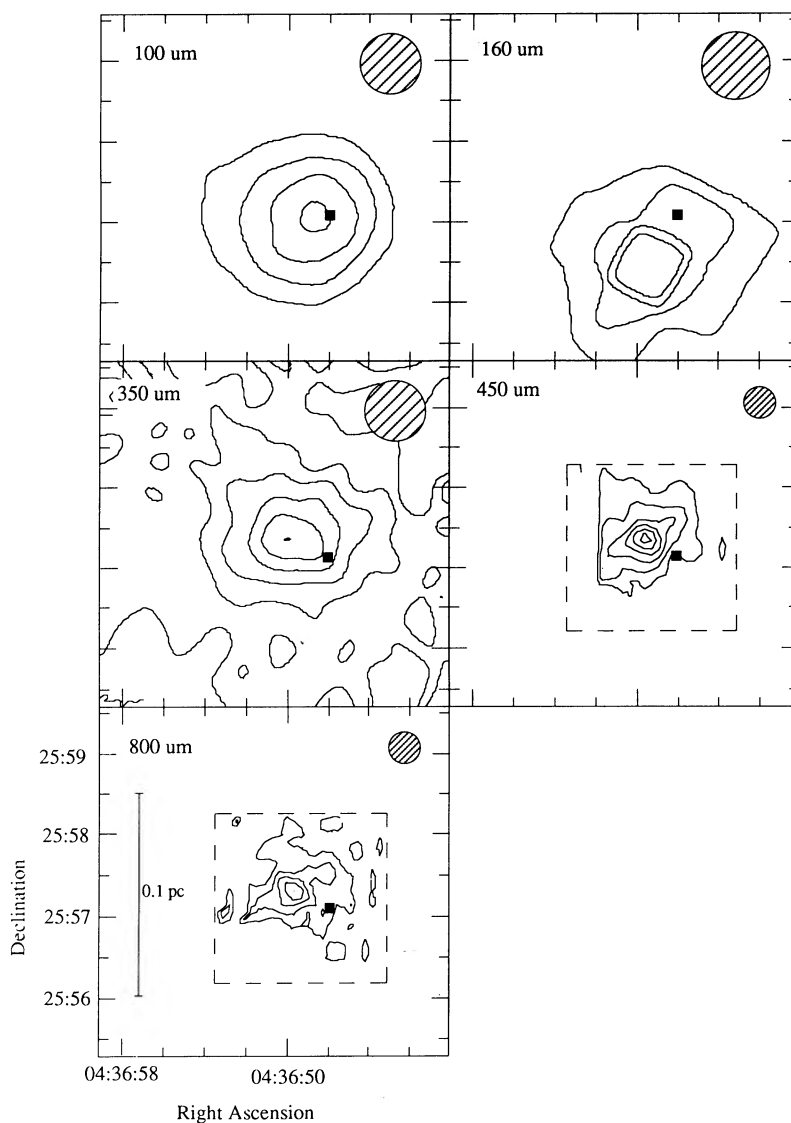

FIG. 5.—Maps of L1527 at 100, 160, 350, 450, and 800 μm. Labels are the same as in Fig. 3. Lowest contour level and contour increments are 10 Jy beam^{-1} and 10 Jy beam^{-1} for the 100 and 160 μm maps, 2.0 Jy beam^{-1} and 2.0 Jy beam^{-1} for the 350 μm, 0.5 Jy beam^{-1} and 0.5 Jy beam^{-1} for the 450 μm map, and 0.1 Jy beam^{-1} and 0.1 Jy beam^{-1} for the 800 μm map. Contours in the 160 μm map appear to be boxy because the source was not well-sampled at this wavelength. Filled squares mark the *IRAS* Point Source position. The position at 160 μm is different from the position determined from the rest of the maps of L1527 probably because of guiding problems during the observation.
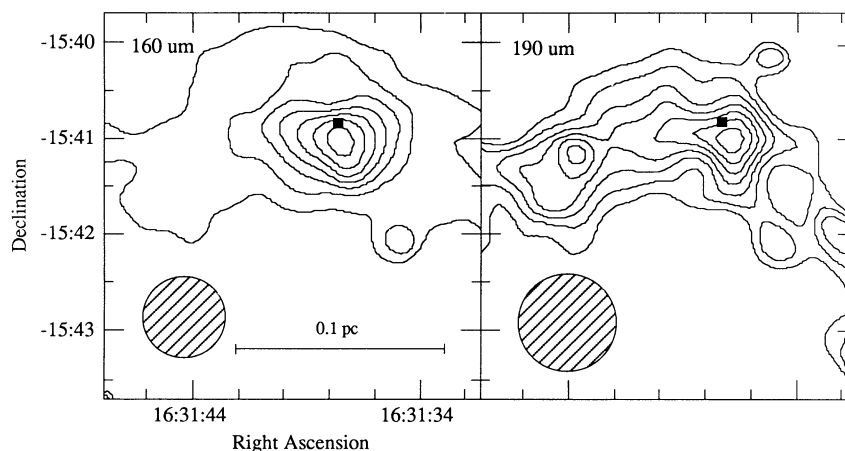
FIG. 6.—Maps of L43 at 160 and 190 μm. Labels are the same as in Fig. 3. Lowest contour level and contour increments are 10 Jy beam^{-1} and 10 Jy beam^{-1} for the 160 μm map and 5 Jy beam^{-1} and 5 Jy beam^{-1} for the 190 μm map. Filled squares mark the *IRAS* Point Source position.

fitting are given in Table 4. In all cases, the FWHM major axis of the fit exceeds the FWHM beam size of the observation, and in only six of 26 cases is the FWHM minor axis equal to or smaller than the beam size of the observation. None of the minor axes is less than 90% of the beam size. The fits are worst at 190 and 350 μm, where the intensity distribution for many sources is clearly not an elliptical Gaussian. At these wavelengths, extended emission is present, but it is not well-centered on the emission peak. Extended emission is present at all wavelengths longer than 100 μm.

Since we have observations of the same sources at several different wavelengths, we can study how the underlying source intensity profile depends on the wavelength and beam size of each observation. The data clearly exclude sources which have constant size with wavelength. At 100 μm the sources are virtually unresolved, while at larger wavelengths and with larger beams, significant structure is visible. Sources with constant size as a function of wavelength would be most clearly resolved in our smallest beams, which is not the case for the data presented here.

However, the size cannot be a monotonically increasing function with wavelength, as one might naively expect. The
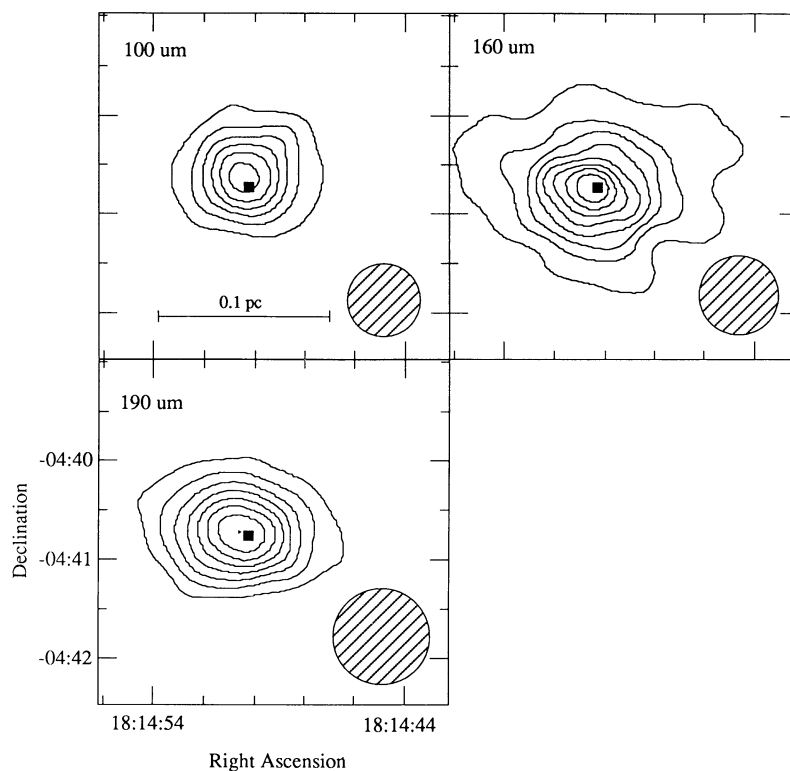

FIG. 7.—Maps of L483 at 100, 160, and 190 μm. Labels are the same as in Fig. 3. Lowest contour level and contour increments are 20 Jy beam^{-1} and 20 Jy beam^{-1} for the 100 μm map, 30 Jy beam^{-1} and 30 Jy beam^{-1} for the 160 μm map, 20 Jy beam^{-1} and 20 Jy beam^{-1} for the 190 μm map. Filled squares mark the *IRAS* Point Source position.
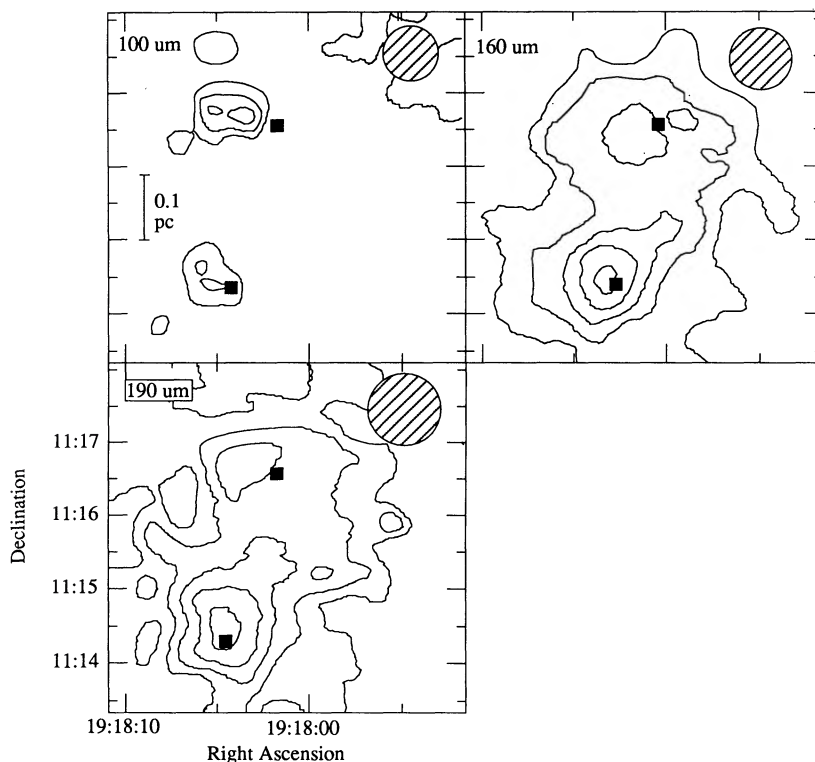
FIG. 8.—Maps of L673A and B at 100, 160, and 190 μm. Labels are the same as in Fig. 3. Lowest contour level and contour increments are 5 Jy beam^{-1} and 5 Jy beam^{-1} for the 100 μm map, 10 Jy beam^{-1} and 10 Jy beam^{-1} for the 160 and 190 μm maps. Filled squares mark the $IRAS$ Point Source position.

standard picture of low-mass star formation—that of a centrally condensed core surrounding a prestellar object—places cooler material farther from the central source. One might expect that the long-wavelength data, which is sensitive to cooler material, will indicate a larger size than an observation made at a shorter wavelength. However, our longest wavelength data, that taken with the JCMT, shows smaller source sizes than the 190 and 350 μm measurements, even after the difference in beams is taken into account. The largest sizes appear to be found not at the extreme long wavelengths, but rather at 190 and 350 μm.

In addition to our result that the 800 μm data show smaller intrinsic source size than at 190 or 350 μm, we also find that the estimated source size is always confined to a small multiple of the beamsize; 24 of 27 maps have estimated source sizes between 1 and 2 times the beam width and all 27 maps have sizes smaller than 4 times the beam width (see Fig. 11). This result cannot be due to sensitivity limitations, as the half-maximum intensity level exceeds 4 σ for all but nine of the 27 fits in Table 4.

The mean major axis of the elliptical Gaussian fit is 1.8 $\pm$ 0.7 times the beam and the mean minor axis is 1.4 $\pm$ 0.6 times the beam. It appears that the underlying intensity profile has no well-defined scale size and that the derived source sizes are a function of the beam size of the measurement. The observations which were made using the largest beams, the 160 (50″)
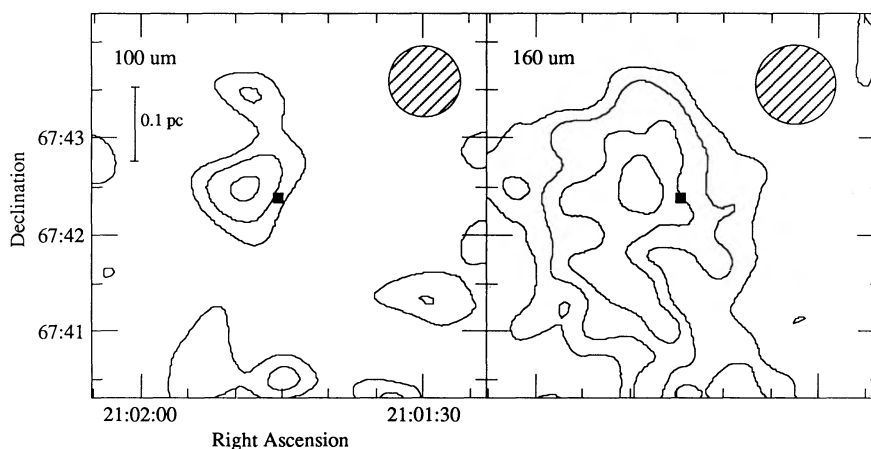

FIG. 9.—Maps of L1172A at 100 and 160 μm. Labels are the same as in Fig. 3. Lowest contour level and contour increments are 3 Jy beam^{-1} and 3 Jy beam^{-1} for the both maps. Filled squares mark the $IRAS$ Point Source position.
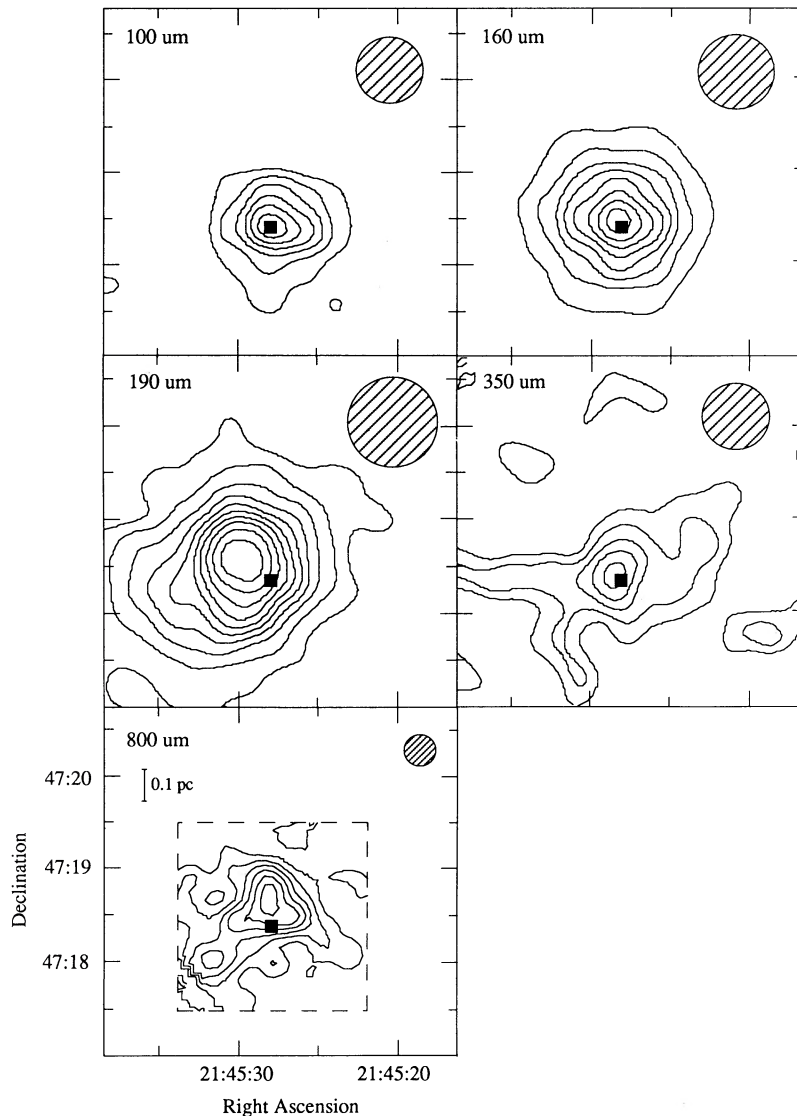
FIG. 10.—Maps of L1031B at 100, 160, 190, 350, and 800 μm. Labels are the same as in Fig. 3. Lowest contour level and contour increments are 10 Jy beam^{-1} and 10 Jy beam^{-1} for the 100, 160, and 190 μm maps, 1.0 Jy beam^{-1}, and 1.0 Jy beam^{-1} for the 350 μm and 0.05 Jy beam^{-1} and 0.05 Jy beam^{-1} for the 800 μm map. Filled squares mark the *IRAS* Point Source position.

and 190 (58″) maps, generally produce the largest estimates of the source sizes. Such a dependence on beam size is indicative of scale-free structure.

A specific intensity distribution which varies as a power law in projected radius can produce this scale-free structure. To estimate how a power-law intensity distribution might appear when observed with a Gaussian beam, we have taken power-law intensity distributions ($I_\nu \propto \omega^{-\alpha}$), with inner and outer cutoffs[4] at 100 A.U. and 10000 A.U., respectively, and convolved them with Gaussians corresponding to the instrumental beam widths used. The resulting flux density profiles were then fitted by Gaussians. We find that for a broad range of power-law indices, the convolved output can be well fitted by a

Gaussian with FWHM size 10%–80% larger than the original beam size. Furthermore, the Gaussian fit to the convolved map is quite good. Only at distances greater than one beam size from the source center (i.e., at a flux level equal to 6% of peak) does the fit break down.

In a companion paper, Adams (1991) presents an analytic approximation of the output image profile at large projected radii from the central source. He also discusses how the observed image profile might be used to determine the underlying physical structure of the protostellar envelope. In § 4, we will use our data and this model to estimate the temperature and density structure of several cores.

3.2. *Shapes*

We find that although the emission regions are somewhat circular is most cases, there are significant departures from purely circular shapes. The aspect ratios of the maps range from 1.0 to 2.0, with a mean of 1.3. The 100 μm observations have aspect ratios close to 1.0, with the exception of L1172A

---

[4] The inner and outer cutoffs were chosen such that the convolution of the power-law profile with a Gaussian beam of FWHM ∼ 5000 A.U. would not be sensitive to their values. The intensity distribution at radii smaller than the inner cutoff radius was assumed to be constant with a value equal to the intensity at the cutoff radius.

TABLE 4

GAUSSIAN FITS TO EMISSION REGIONS

Source	λ (μm)	Peak Flux (Jy beam^{-1})	Peak R.A.[a]	Peak Decl.[a]	Fit Flux (Jy beam^{-1})	Fit R.A.[a]	Fit Decl.[a]	Major Axis	Minor Axis	P.A.	Baseline Level (Jy beam^{-1})	Aspect Ratio
L1489	100	47	-9"	-9"	53.4 (1.1)	-8"	-9"	54".5 (1.1)	51".8 (1)	8° (20°)	-3.2 (0.4)	1.05 (0.04)
	160	46	-5	-13	37 (0.7)	0	-4	78 (1.5)	78 (1.4)	24 (0.1)	4 (0.3)	1.00 0.04
	350[b]	4.8	12	-9	5.2 (0.1)	27	14	158 (3.6)	132 (2.3)	147 (5.9)	-0.8 (0.04)	1.20 (0.05)
	800	0.3	0	-5	0.44 (0.03)	7	1	84 (5.6)	46 (3)	45 (1.9)	-0.16 (0.03)	1.83 (0.24)
L1535	100	24	21	1	28 (1)	25	8	49 (2)	42 (2)	30 (14)	-0.1 (0.4)	1.16 (0.10)
	160	46	29	1	33 (1)	37	15	104 (3)	91 (2)	24 (13)	4.5 (0.4)	1.14 (0.06)
L1527	100	42	7	-2	47 (1)	15	-3	90 (1)	85 (1)	109 (7)	-6.1 (0.2)	1.06 (0.02)
	160	69	18	-34	56 (2)	15	-33	73 (2)	56 (2)	134 (5)	14 (1)	1.30 (0.08)
	350	12	27	17	8.5 (0.1)	24	21	85 (1)	67 (1)	83 (3)	2.8 (0.1)	1.43 (0.04)
	450	3.2	23	16	2.1 (0.1)	22	18	38 (1)	25 (2)	120 (3)	0.6 (0.1)	1.51 (0.16)
	800	0.5	23	16	0.33 (0.01)	20	19	37 (3)	22 (1)	115 (3)	0.09 (0.01)	1.67 (0.21)
L43	160	75	-3	-8	62 (1)	0	-8	70 (1)	49 (2)	81 (4)	8.0 (0.7)	1.43 (0.08)
	190	38	-10	-10	31 (1)	7	-5	94 (1)	54 (2)	74 (1)	-0.1 (0.2)	1.75 (0.08)
L483	100	200	-3	9	195 (2)	-4	13	54 (1)	48 (1)	99 (5)	0.7 (0.8)	1.11 (0.04)
	160	390	-1	7	316 (4)	-1	3	62 (1)	50 (1)	87 (3)	35 (2)	1.25 0.04
	190	230	1	-12	232 (2)	1	6	70 (1)	52 (1)	84 (2)	-9 (1)	1.33 (0.04)
L673B	100	19	31	9	...	...	...	...	...	...	...	...
	160	33	25	-4	32 (1)	24	-76	153 (5)	132 (3)	77 (9)	3.4 (0.4)	1.16 (0.06)
	190	35	29	-43	28 (1)	12	-60	123 (2)	87 (1)	62 (1)	4 (1)	1.41 (0.04)
L673A	100	11	18	30	19 (1)	12	9	94 (5)	63 (3)	136 (6)	-9.3 (0.4)	1.50 (0.15)
	160	56	-1	14	39 (1)	-4	5	81 (2)	53 (1)	137 (3)	13 (1)	1.54 (0.07)
	190	53	0	17	42 (1)	-7	8	102 (3)	73 (2)	167 (4)	8.2 (0.5)	1.40 (0.08)
L1172A	100	9.6	27	6	11 (1)	20	14	90 (2)	51 (1)	164 (1)	-2.7 (0.1)	1.77 (0.07)
	160	8.6	36	-52	...	...	...	...	...	...	...	...
L1031B	100	67	-1	13	60 (1)	-4	14	51 (1)	44 (1)	79 (5)	2.3 (0.4)	1.18 (0.05)
	160	86	-3	15	74 (1)	4	16	64 (1)	64 (1)	65 (9)	4.0 (0.3)	1.05 (0.03)
	190	110	19	21	99 (1)	20	17	78 (1)	66 (1)	136 (4)	7.8 (0.6)	1.18 (0.03)
	350	5.4	8	8	4.5 (0.2)	1	15	97 (2)	67 (4)	103 (5)	-0.3 (0.1)	1.45 (0.12)
	800	0.3	8	10	0.29 (0.02)	3	6	42 (3)	39 (3)	110 (18)	0.04 (0.02)	1.08 (0.16)

NOTE.—Numbers in parentheses are errors in the last digit quoted. P.A. = position angle of the Gaussian fit in degrees east of north.
[a] Offsets in right ascension and declination are calculated relative to the values in Table 1A.
[b] This map was convolved to a beam size of 50" to enhance the signal-to-noise ratio.

which is not well fitted by an elliptical Gaussian. The longer wavelength maps generally have higher aspect ratios. This trend is not a result of differing beam sizes, since the long-wavelength KAO maps generally have larger aspect ratios than the 100 μm maps, despite their larger beam sizes.

For many of the sources, the estimated position angle from the Gaussian fits is independent of wavelength. For L1535, L43, L483, L673B, and L673A, the position angle agrees to within 30° over the wavelength range observed. L1489, L1527, and L1031B show similar agreement at most wavelengths—the discrepant position angles are primarily from fits to nearly round images which are not well constrained.

The shape of the far-infrared emission matches reasonably well with observations of dense gas associated with these sources. Here we compare our far-infrared maps with maps of the 1.3 cm $(J, K) = (1, 1)$ emission line of NH_3 made by Benson & Myers (1989; L1489, L1527, L43, L1172A, and L1031B), Ungerechts, Walmsley, & Winnewisser (1982; L1535), and Benson (1990; L483, L673A, B). All of these maps, with the exception of L1535, were made with the 37 m Haystack Observatory antenna, with a FWHM beam size of 88". The L1535 map was made with the Effelsberg 100 m antenna with a FWHM beam size of 40". In all cases, the NH_3 emission is more extended than the far-infrared emission.

Figure 12 shows the half-power contour from either our 160, 190, or 350 μm maps superposed on the half-power contour from the associated ammonia map for each source. The far-infrared half-power contour is contained within the ammonia contour in half of the maps presented in Figure 12. Only when the associated IR point source is located outside of the ammonia contour is the ammonia distribution significantly different from that of the far-infrared (e.g., L1489, L1535, and L673). In L43, L483 and L1031B, the ammonia and far-infrared half-power contours have similar shape.

Benson & Myers (1989) have calculated the size, aspect ratio, and position angle of the NH_3 emission with Gaussian fits to their observations. For the remaining three sources, we have estimated the position angle and aspect ratio from examination of the published maps. In six out of the eight cases shown in Figure 12, the difference between the position angle of the ammonia emission and that of the far-infrared emission is less than 20°. Five of the eight have aspect ratios which differ by less than 0.3.

Pendleton et al. (1990) have noticed a correlation between regions of far-infrared emission and NH_3 detections in the star-forming dark cloud B5. L43 and L673 resemble B5 in this respect, since the NH_3 and far-infrared maps show similar elongation and/or multiple peaks. The observations presented here indicate that such a correlation is the norm for low-mass star formation regions. Furthermore, Myers et al. (1991) have noticed a similarity between the shapes of NH_3, CS, and $C^{18}O$ contours for a large number of low-mass star formation regions, despite the rather large range of areas and densities traced by these molecular constituents. Considering these results in conjunction with our far-infrared images, we suggest that even the material closely associated with forming stars has a shape similar to that of the surrounding cloud on a size scale some 10 times greater.
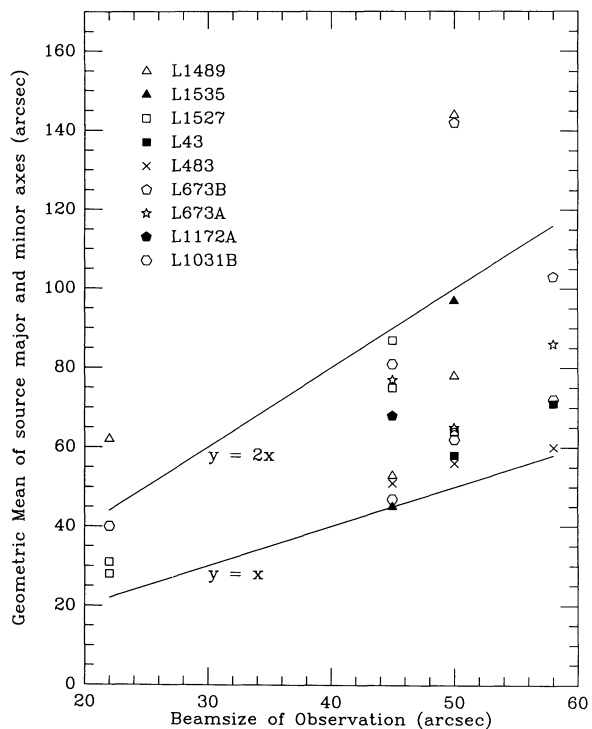
FIG. 11.—Source size vs. beam size for 27 maps in our survey. Source size is denoted as the geometric mean of the major and minor axes of the Gaussian fit to each map. Only three maps have source sizes greater than 2 times the beam size.

The departures from spherical symmetry seen here are on a size scale of 0.1 pc—much larger than the circumstellar scale where an anisotropic density distribution was inferred from the complete spectral energy distributions in Paper I. Even if the observed aspect ratios at 0.1 pc are maintained down to circumstellar scales, an anisotropic density distribution with an aspect ratio of ~ 2 would not sufficiently lower the total obscuration to account for the near-infrared excess discussed in Paper I. A greater column density contrast that the factor of ~ 2 inferred from these large-scale observations is required.

4. DISCUSSION

Since the emission profiles of many of these regions are extended in the far-infrared and submillimeter, we can examine the properties of the cores as a function of spatial position. In this section, we first discuss the far-infrared and submillimeter spectrum as a function of position for L1489 and L1527. We then compare the observed spatial profile of L1489, L1527, and L1031B at several submillimeter wavelengths with theoretical estimates of the flux from a core with power-law density and temperature distributions.

4.1. Spectrum of Extended Emission

The extended emission around these sources appears to have a spectral energy distribution different from that measured directly along the line of sight toward the central sources. Figures 13 and 14 show the spectrum of the on-source emission (i.e., the emission from the center beam), along with the spectra for positions offset by 60" for two of our sources, L1489 and L1527. These sources were selected because they are well mapped over the entire wavelength range discussed in this work. For this analysis, all of the maps were convolved to have
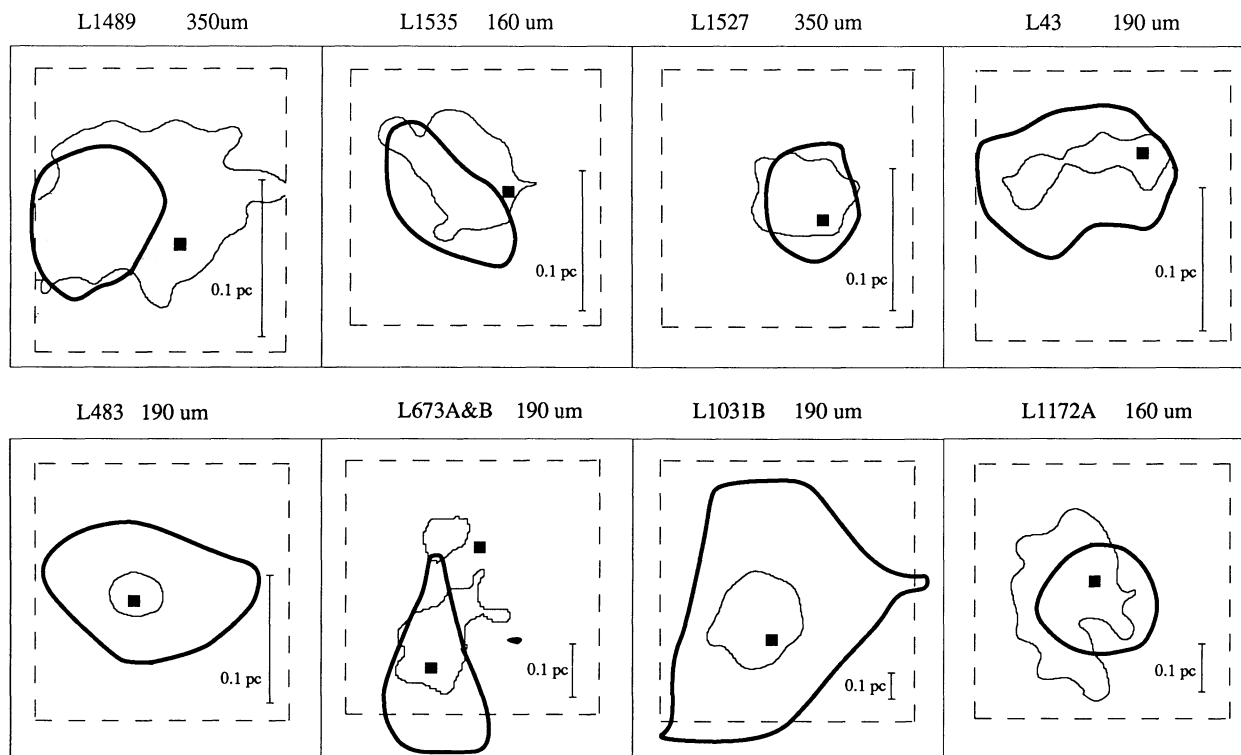

FIG. 12.—Comparison between the half-power contours of NH$_3$ $(J, K) = (1, 1)$ antenna temperature with the half-power contours from our far-infrared emission maps. Dotted lines delineate the extent of the region mapped in the far-infrared. In all cases the NH$_3$ was mapped over a larger area.
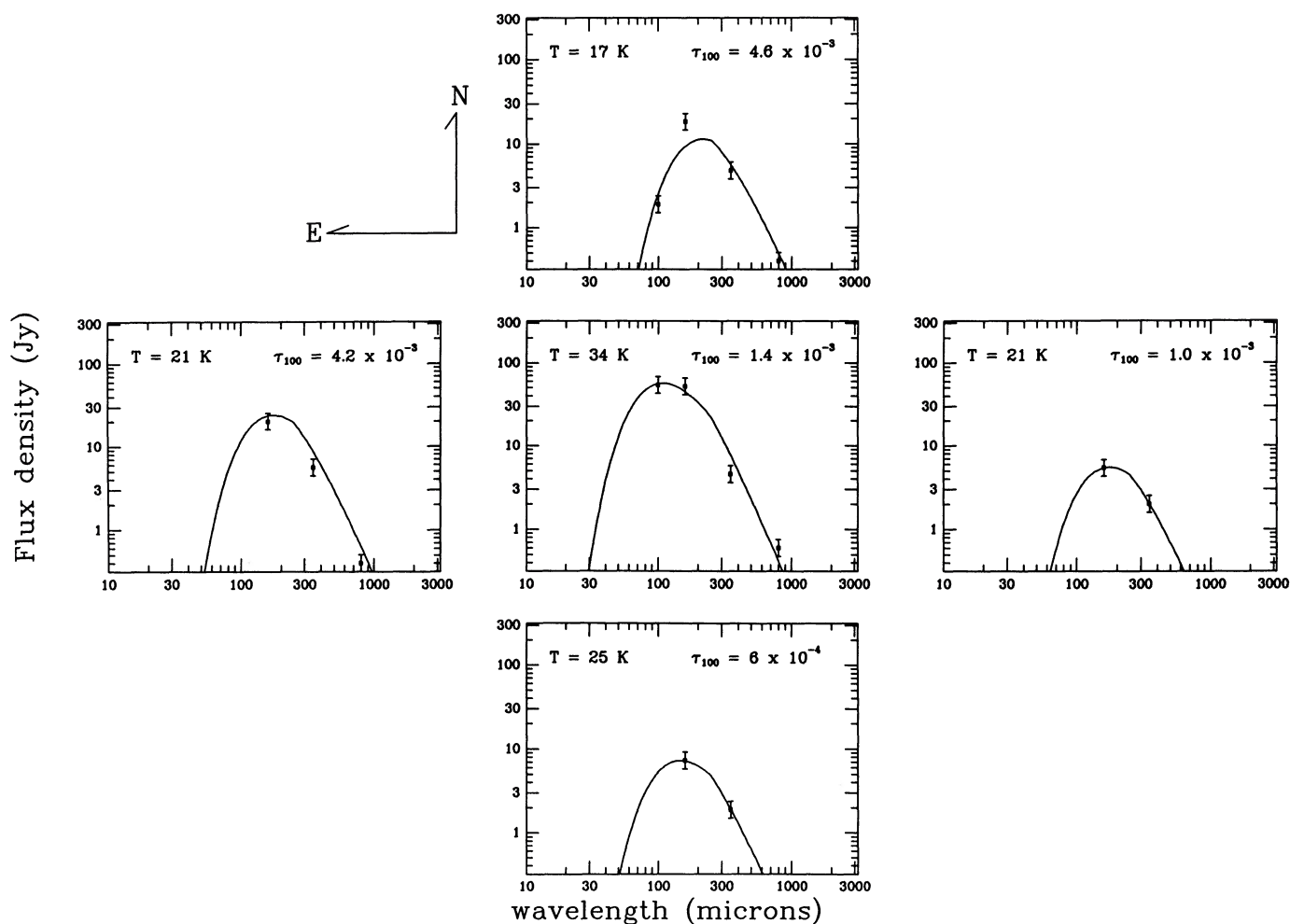
FIG. 13.—Far-infrared spectra toward L1489 at one on-source position and four off-source positions located 60″ in projection from the central source. Fits to the data are optically thin blackbodies, with an emissivity law described by Hildebrand (1983). Estimated temperature in kelvins is listed in the upper left of each box, and the estimated optical depth at 100 μm is listed in the upper right.

60″ effective beam sizes. Although the fluxes in the offset spectra are all weaker than the corresponding fluxes toward the central source, the short-wavelength flux (especially at 100 μm) is the most reduced.

The on-source spectrum of L1489 has a higher temperature than the off-source positions. A best-fit optically thin blackbody spectrum with a dust emissivity law from Hildebrand [1983; $\kappa_v \propto v^{\beta}$, where $\beta = 1$ for log $(v) > 12.1$ and $\beta = 2$ for log $(v) < 12.1$] has a temperature of 34 K on-source, while the warmest off-source position has a temperature of 25 K and the others are nearer 20 K. In contrast, the on-source spectrum of L1527 has a fit temperature of 26 K, and the off-source positions have slightly lower fit temperatures of 20–25 K. Since the fit temperature for the on-source beam toward L1527 is only slightly different from the temperatures derived from the off-source beams, we conclude that the embedded source in L1527 has not warmed a large volume of the surrounding dust. The dust contained within the beam centered on the infrared source in L1489, however, appears to have been heated to a temperature higher than that of the surrounding material. Ladd et al. (1988) have previously suggested that although both are clearly class I sources (in the language of Adams, Lada, & Shu 1987), L1527 is younger than L1489; perhaps envelope material is heated more in the later stages of star formation.

Alternatively, the optical depth of the cold material in L1527 may be so large that it obscures the warmer interior regions even in the submillimeter.

The 100 μm beam-averaged optical depths derived from the blackbody fits are also listed in Figures 13 and 14. The largest optical depth on this scale is not located at the emission peak for either source, but is offset by at least one beam. The position of peak optical depth is also the position of the lowest color temperature in both maps. Assuming a ratio of visual extinction A_v to optical depth at 100 μm of 1000, we find that the beam-averaged visual extinction is within a factor of 2 of the values deduced from NH_3 observations (Benson & Myers 1989) and star counts (Cernicharo, Bachiller, & Duvert 1985).

The color temperature and opacity calculated for the off-source positions are probably reasonable estimates of the physical conditions in the outer parts of the core, since at sufficiently large distances from the central source the temperature probably does not vary much within the beam. Therefore, a single-temperature model may be adequate. However, the values derived from the on-source beams are somewhat more suspect. The beam-averaged optical depth determined here ($A_v \sim 5$) is considerably smaller than the central ray optical depth we estimated from the complete spectral energy distribution of L1489 ($A_v = 53$) and L1527 ($A_v \sim 2000$) in
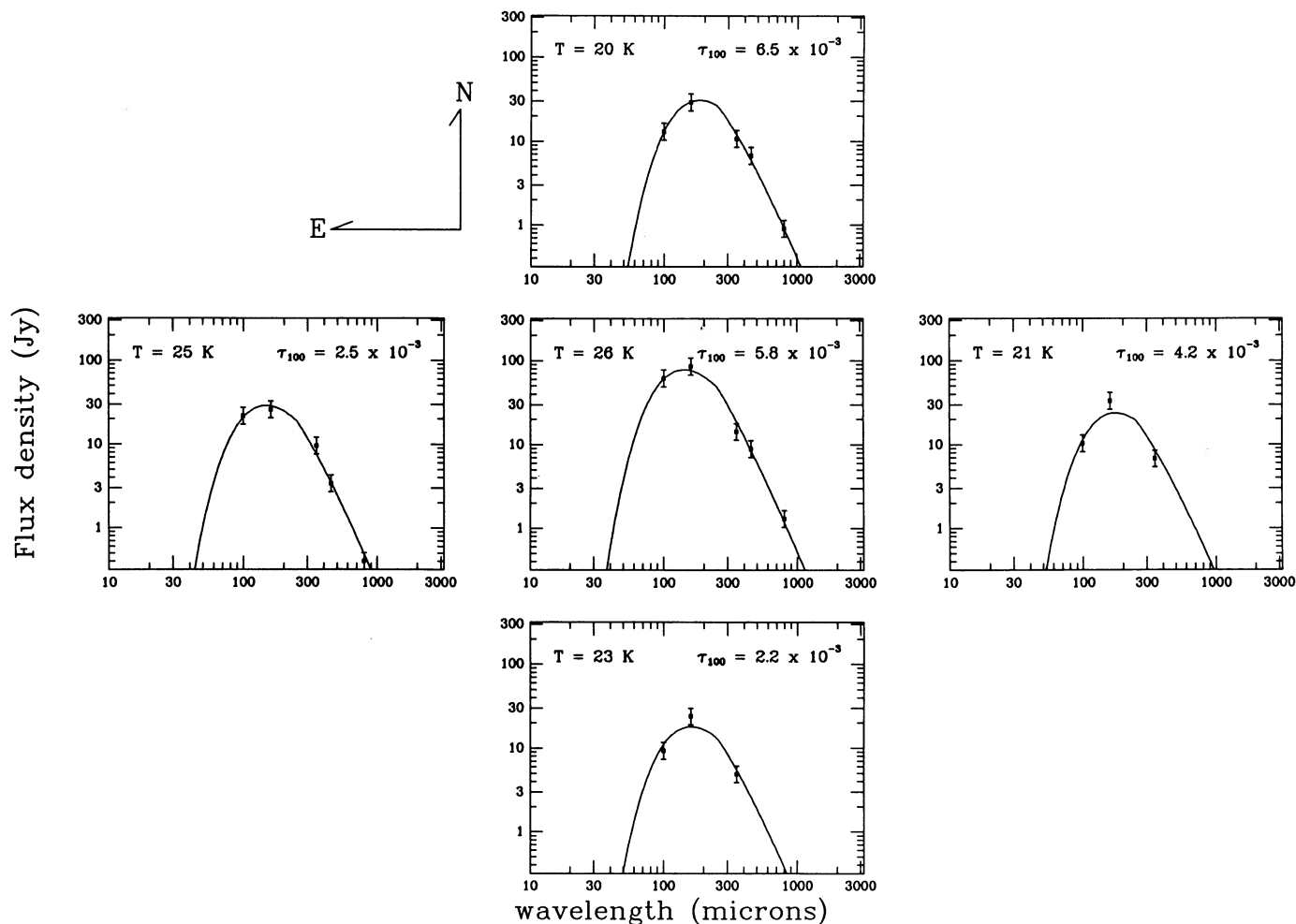
FIG. 14—Far-infrared spectra toward L1527 at one on-source position and four off-source positions located 60″ in projection from the central source. Fits to the data are optically thin blackbodies, with an emissivity law described by Hildebrand (1983). Estimated temperature in kelvins is listed in the upper left of each box, and estimated optical depth at 100 μm is listed in the upper right.

Paper I. Our long-wavelength data do not sample effectively the small spatial scales and high temperatures characteristic of most of the optical depth in the core. Within the central beam the temperature and density structure are quite likely very complex, and any beam-averaged value for the color temperature or the opacity probably does not represent the average dust temperature or total optical depth within the beam. A more accurate estimate of the temperature and density in the inner regions can be obtained with higher resolution infrared imaging or by relying on models of the physical core structure.

4.2. Flux Profiles

Figure 15 shows the size of the emission region as a function of flux level for L1527 at four wavelengths. The size of the map at each flux level is defined as the radius of the circle with the same area as enclosed by that isointensity contour. This method of display compresses the information in the maps into a single dimension, but averages the data in a different manner from an azimuthal average. The profiles are plotted in units of the appropriate beam sizes.

At the shortest wavelength, 100 μm, the source has a radial profile which is very close to Gaussian. However, at longer wavelengths, the profile becomes progressively less Gaussian and more like a power law. At the longest wavelength, 800 μm, the radial profile is well approximated by a power law in intensity. This effect is not the result of different beam sizes, since Figure 15 is plotted in units of the half-peak beam width at the particular wavelength of the figure. The power law seen at longer wavelengths extends over approximately the same number of beam widths ($\sim$1–2) as the Gaussian seen at shorter wavelengths.

The power-law flux profile observed at 800 μm is suggestive of a power-law intensity distribution. Such a distribution can be produced by a power-law distribution of temperature and density in an optically thin core in the Rayleigh-Jeans limit. While the Rayleigh-Jeans approximation is just marginally valid for 800 μm observations of $\sim$30 K dust, it is clearly violated at shorter wavelengths and a more robust approximation to the emitted intensity profile is required.

4.3. Determining Temperature and Density Structure

In a companion paper Adams (1991) derives an approximate analytic form for the projected spatial intensity distribution for a protostellar envelope whose density and temperature distributions vary as power laws in radius. He also shows that
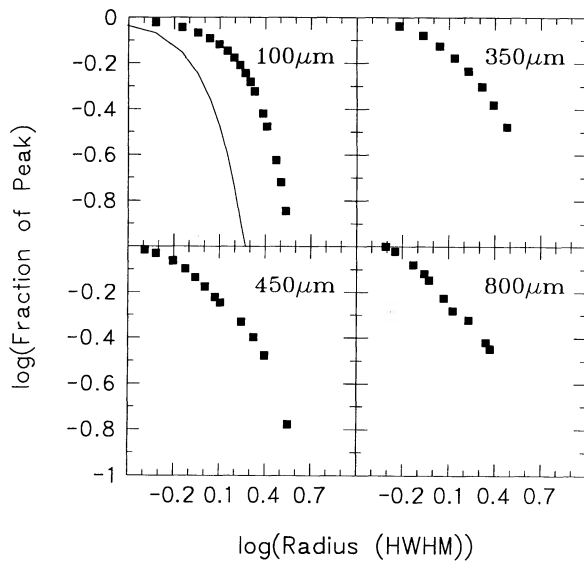
FIG. 15.—Size of the emission region as a function of flux level for L1527 at four wavelengths. Size of the map at each flux level is defined as the radius of the circle with the same area as enclosed by that isointensity contour. Profiles are plotted in units of the beam size of each observation. Solid line on the 100 μm plot shows a Gaussian beam.

spatially resolved, multiwavelength observations at submillimeter wavelengths can be used to constrain the density and temperature power-law indices [hereafter p and q, respectively, where $\rho(r) = \rho_0(r_0/r)^p$ and $T(r) = T_0(r_0/r)^q$]. In particular, the ratio of flux density at the center (on-source) position, $S_\nu(0)$, to the flux density at a position offset by one full beam width from the center, $S_\nu(B)$, can be related to the effective power-law index m of the specific intensity profile by

$$\frac{S_\nu(B)}{S_\nu(0)} = \gamma_\nu\left(\frac{2}{8\ln 2}\right)^{m/2}\frac{1}{\Gamma_\nu(1-m/2)}$$
$$\times\left[1 + \frac{m^2}{16\ln 2} + \frac{m^2(m+2)^2}{512(\ln 2)^2} + \cdots\right], \quad (1)$$

where γ_ν is a correction term which takes into account the deviation of I_ν from a single power law (see Appendix B to Adams 1991), and where we have kept the first three terms in an asymptotic series. To leading order, m can be related to p and q by

$$m = p + qQ - 1 + \cdots, \quad (2)$$
where

$$Q = \frac{xe^x}{e^x - 1} \quad \text{and} \quad x = \frac{h\nu}{kT_0}\left(\frac{B}{r_0}\right)^q,$$

and h is Planck's constant, k is Boltzmann's constant, B is the physical FWHM size of the beam on the source, and $T_0 r_0^q$ is a temperature normalization factor where T_0 is the temperature at radius r_0 from the center of the core. Note that Q is a function of wavelength. Since the intensity profile can be characterized by just three quantities (p, q, and T_0), observations at three different wavelengths are necessary (and sufficient) to estimate these parameters.

We have calculated the density and temperature power-law indices for three sources in our sample (L1031B, L1489, and L1527). These sources were chosen because we have at least

three well-sampled maps of each at wavelengths longer than the peak of its spectral energy distribution. In this first attempt at determining the temperature and density structure, each map was azimuthally averaged about the peak pixel position to enhance the off-peak signal-to-noise ratio. We then calculated $S_\nu(B)/S_\nu(0)$ for each source in three long-wavelength maps. These ratios were then compared to ratios determined from a grid search of (p, q, T_0) parameter space.

The best-fit parameters are listed in Table 5. The uncertainties reflect the full range of variation in each parameter which still yields an acceptable solution (defined by $\chi^2 \lesssim 2$). For L1489 and L1527, p and q appear to be weakly constrained and the value of T_{1000} (the temperature at a radius of 1000 A.U.) is virtually unconstrained between our limits of 20 and 200 K. For L1031B, the data and model place no significant constraint on p and q.

The best constrained quantity appears to be the sum $p + q$, which varies less than p and q individually in all three sources. This result is not unexpected, since this analysis is an extension of the Rayleigh-Jeans approximation to shorter wavelengths. In the extreme Rayleigh-Jeans limit, the physical quantity I_ν and hence S_ν depend only on the sum $p + q$ and not on the individual values of p and q. In this formulation, the specific intensity is characterized by the index $m (\simeq p + Qq - 1) + \cdots)$. Since Q varies with wavelength, p and q can be determined independently with multiple wavelength observations. However, Q is a fairly slowly varying function of ν ($Q = 1 \sim 3$ in this regime), so $p + qQ \simeq p + q$, and the sum is more tightly constrained than either individual value.

Although we cannot tightly constrain the value of q, theoretical results indicate that for a wide variety of core density distributions $q \simeq 0.4$, especially in the outer core regions (e.g., Scoville & Kwan 1976; Wolfire & Cassinelli 1986; Adams & Shu 1986). Using this value in conjunction with our result that $p + q = 2.1^{+0.2}_{-0.3}$, we estimate that $p \simeq 1.7 \pm 0.3$ in the spatial range. $0.01 < r < 0.03$ pc. This result indicates that even at these small scales within a dense core, the density gradient is steep.

Other studies of p in dense core regions at larger scales have found generally smaller values. Star counting studies have shown that the density scales with a flatter slope ($p = 1.0–1.3$) on size scales ranging from 0.1–1.0 pc (Stüwe 1990; Cernicharo et al. 1985). Davidson (1987) reports a similar flattening in slope at 0.1 pc scale sizes from CO measurements, and Fuller (1989) calculates a value of 1.4 ± 0.4 for p from $C^{18}O$ and NH_3 observations over 0.1–0.7 pc.

At the smaller scales to which our model results are sensitive, marginally steeper density gradients have been found. Frerking, Langer, & Wilson (1987) estimate p to be 1.8 in the inner 0.5 pc of B335 from infrared and NH_3 observations. More

TABLE 5
DERIVED QUANTITIES FROM FITS TO EXTENDED EMISSION

Core	p	q	T_{1000}	$p + q$
L1489	1.7 ± 0.3	$0.4^{+0.2}_{-0.3}$	80^{+60}_{-40}	2.1 ± 0.1
L1527	$1.5^{+0.8}_{-0.7}$	$0.6^{+0.4a}_{-0.6}$	100^{+200a}_{-80}	$2.1^{+0.2}_{-0.3}$
L1031B[b]	...	...	...	...

[a] This parameter is completely unconstrained by the data. The limits displayed are the limits of the search grid in this parameter.
[b] No parameter set adequately fits the L1031B data [$\chi^2 > 2.5 \,\forall\, (p, q, T_{1000})$]. The best-fit values ($\chi^2 = 2.74$) are $p = 1.9$, $q = 0.3$, and $T_{1000} = 160$. The sum of p and q is 2.2.

recently Butner et al. (1991) have used far-infrared emission profiles to determine the density structure at 0.01 pc scales in L1551 and have found $p = 1.5 \pm 0.3$. Our result, taken in conjunction with these other estimates, is consistent with a steeper density gradient at small-scale sizes around a forming star. These estimated values for p are in reasonable agreement with the theoretically predicted value of $p = 1.5$ for the inner regions of a collapsing isothermal cloud core (Shu 1977).

Yamashita et al. (1990) have performed a similar derivation using submillimeter observations of the massive forming star GGD 27. They find acceptable fits to the extended emission for p in the range 1.6–2.0. Since GGD 27 is 2.2 kpc distant, their results are sensitive only to large linear scales ($r \sim 0.2$ pc). The similarity between their result and the slope we derive for a 5 $L_\odot$ low-mass star suggests that cores forming more massive stars may have structure similar to that of cores forming low-mass stars, although on a larger scale.

The errors on our estimates of $S_\nu(B)/S_\nu(0)$ are large and occasionally exceed 50%, largely because our mapping program was designed to detect the peak flux and not to map fully the extended emission. A dedicated program to observe the extended structure at high spatial resolution and high signal-to-noise ratio at far-infrared and submillimeter wavelengths will significantly reduce the uncertainties in all of the quantities in Table 5. In addition, extended wavelength coverage, especially for the wavelength range 350 μm $< \lambda < 1100$ μm, will further constrain the model parameters (Adams 1991).

5. CONCLUSIONS

1. Far-infrared emission from nine regions forming low-mass stars is resolved by observations with beam widths ranging from 22″ to 58″. The FWHM size of the extended emission regions range from 5.2×10^{16} to 1.3×10^{18} cm. Three sources, L673, L1489, and L43, have two distinct emission peaks at long wavelength. The sizes are neither constant nor simply correlated with wavelength. Rather, they appear to be weakly correlated with the beam size of the observations, suggesting that the underlying specific intensity profile is scale-free. A specific intensity profile which varies as a power law with radius is consistent with the observations.

2. The extended emission regions are not circularly symmetric, but have aspect ratios which range from 1 to 2 with an average of 1.3. The position angles of Gaussian fits to these emission regions correlate well with the position angles determined from molecular observations of dense gas in the lines of NH_3, CS, and $C^{18}O$.

3. In L1489, the spectral energy distribution of the extended emission appears to be colder than the on-source spectral energy distribution. In this case, the extended emission can be fitted by a blackbody with temperature ~ 21 K, while the on-source emission has $T = 34$ K. In L1527 the blackbody temperature is ~ 25 K for both on-source and off-source emission.

4. For L1489 and L1527, the extent of the emission as a function of wavelength is consistent with a model which assumes that the density and temperature of the protostellar envelope vary as a power law in radius through the core. Using this model, we have estimated the values of the power-law indices for both the temperature and density distributions. Their sum is shown to be $2.1^{+0.3}_{-0.3}$. Independent arguments indicate that q has a value close to 0.4; our results therefore suggest that $p = 1.7 \pm 0.3$ in the inner 10^4 A.U. of L1489 and L1527.

REFERENCES

Adams, F. C. 1991, ApJ, 382, 544
Adams, F. C., Emerson, J. P., & Fuller, G. A. 1990, ApJ, 357, 606
Adams, F. C., Lada, C. J., & Shu, F. H. 1987, ApJ, 312, 788
Adams, F. C., & Shu, F. H. 1986, ApJ, 308, 836
Ade, P. A. R., Griffin, M. J., Cunningham, C. T., Radostitz, J. V., Predko, S., & Nolt, I. G. 1984, Infrared Phys., 24, 403
Beichman, C. A., Myers, P. C., Emerson, J. P., Harris, S., Mathieu, R., Benson, P. J., & Jennings, R. E. 1986, ApJ, 307, 337
Benson, P. J. 1990, private communication
Benson, P. J., & Myers, P. C. 1989, ApJS, 71, 89
Butner, H. M., Evans, N. J., Lester, D. F., Levreault, R. M., & Strom, S. E. 1991, ApJ, in press
Cernicharo, J., Bachiller, E., & Duvert, G. 1985, A&A, 149, 273
Davidson, J. A. 1987, ApJ, 315, 602
Frerking, M. A., Langer, W. D., & Wilson, R. W. 1987, ApJ, 313, 320
Fuller, G. A. 1989, Ph.D. Dissertation, Department of Astronomy, University of California, Berkeley
Griffin, M. J., Ade, P. A. R., Orton, G. S., Robson, E. I., Gear, W. K., Nolt, I. G., & Radostitz, J. V. 1986, Icarus, 65, 244
Harper, D. A., Hildebrand, R. H., Steining, R., & Winston, R. 1976, Appl. Optics, 15, 53
Haslam, C. G. T. 1974, A&AS, 15, 333
Hildebrand, R. H. 1983, QJRAS, 24, 267
———. 1986, Opt. Eng., 25, 323

Ladd, E. F., Adams, F. C., Casey, S., Davidson, J. A., Fuller, G. A., Harper, D. A., Myers, P. C., & Padman, R. 1991, ApJ, 366, 203 (Paper I)
Ladd, E. F., Myers, P. C., Casey, S. C., Harper, D. A., Davidson, J. A., Benson, P. J., & Levreault, R. M. 1988, in Submillimeter Astronomy, ed. G. D. Watt & A. S. Webster (Dordrecht: Kluwer), 35
Larson, R. B. 1969, MNRAS, 145, 271
Lasenby, A., & Hills, R. E. 1991, in preparation
Myers, P. C., Fuller, G. A., Goodman, A. A., & Benson, P. J. 1991, ApJ, 376, 561
Pendleton, Y., Davidson, J., Casey, S., Harper, A., Pernic, R., & Myers, P. 1990, in Submillimeter Astronomy, ed. G. D. Watt & A. S. Webster (Dordrecht: Kluwer), 189
Sandell, G. S. 1989, private communication
Scoville, N. Z., & Kwan, J. 1976, ApJ, 206, 718
Shu, F. H. 1977, ApJ, 214, 488
Shu, F. H., Adams, F. C., & Lizano, S. 1987, ARA&A, 25, 23
Stüwe, J. A. 1990, A&A, 237, 178
Ulich, B. L. 1981, AJ, 86, 1619
Ungerechts, H., Walmsley, C. M., & Winnewisser, G. 1982, A&A, 111, 339
Walker, C. K., Adams, F. C., & Lada, C. J. 1990, ApJ, 349, 515
Wolfire, M. G., & Cassinelli, J. P. 1986, ApJ, 310, 207
———. 1987, ApJ, 319, 850
Yamashita, T., Sato, S., Kaifu, N., & Hayashi, S. S. 1990, ApJ, 365, 615